



Quantifying battery stress factors: An intuitive generic model for calendar and cycle aging simulation using time series analysis

Samira Kiefer^{a,b,c} ,* Maximilian Bruch-Rosar^a , Hans-Martin Henning^{a,c} , Magdalena Graczyk-Zajac^{b,d}

^a Department of Electrical Energy Storage, Fraunhofer Institute for Solar Energy Systems ISE, Heidenhofstr. 2, Freiburg, 79110, Germany

^b Research & Development, EnBW Energie Baden-Württemberg AG, Durlacher Allee 93, Karlsruhe, 76131, Germany

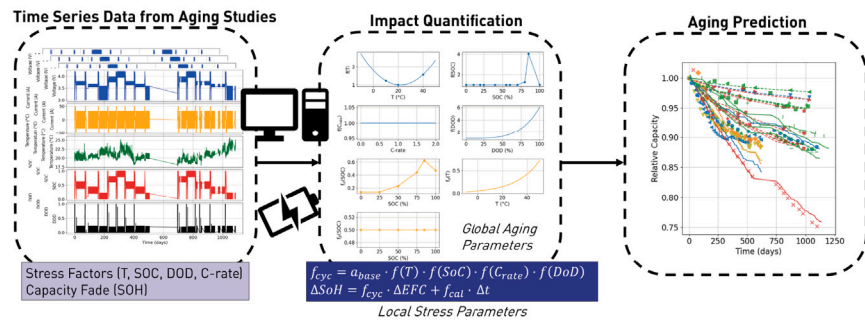
^c Department of Sustainable Systems Engineering (INATECH), Albert-Ludwigs-Universität Freiburg, Emmy-Noether Str. 2, Freiburg, 79110, Germany

^d Institute of Materials Science, Technical University of Darmstadt, Otto-Berndt-Str. 3, Darmstadt, 64287, Germany

HIGHLIGHTS

- Novel empirical aging model based on stress factors.
- Stress factor identification based on time series data.
- Intuitive and interpretable aging parameters.
- Rapid assessment of key factors contributing to aging.

GRAPHICAL ABSTRACT



ARTICLE INFO

Keywords:

Lithium-ion battery
Battery aging
Aging model
Stress factor identification

ABSTRACT

This study introduces a comprehensive and generic aging model that disentangles and quantifies the isolated effects of individual stress factors on lithium-ion battery degradation. Unlike traditional empirical or semi-empirical models, which often combine stress factors into aggregate predictions, the proposed framework leverages time series analysis to resolve the distinct contributions of temperature, state of charge (SOC), depth of discharge (DOD), and current rate (C-rate). This allows not only the capture of overall degradation trends but also the interpretable parameterization of stress-dependent contributions across the operating ranges of NMC cells. The model achieves high predictive accuracy, with a mean absolute error (MAE) of 1.10% for training and 0.61% for validation against data from realistic load profiles. Key findings reveal that the SOC plays a crucial role in battery aging, particularly at elevated levels, with diminishing negative effects observed beyond 85% SOC. In addition, DOD emerged as the most significant factor, with higher DOD levels correlating with accelerated aging, likely due to mechanical stresses impacting electrode integrity. The analysis showed that while SOC consistently contributes to aging, the C-rate exhibited minimal influence within the tested parameters. This study emphasizes the importance of understanding these aging factors for developing effective battery management strategies. Despite the model's predictive performance, several limitations were identified, including challenges in representing extreme conditions and accurately modeling non-linear capacity fade. Understanding these limitations is essential for enhancing the model's applicability and reliability in real-world scenarios. Overall, this approach advances beyond cumulative modeling frameworks by offering

* Corresponding author at: Department of Electrical Energy Storage, Fraunhofer Institute for Solar Energy Systems ISE, Heidenhofstr. 2, Freiburg, 79110, Germany.

E-mail address: samira.kiefer@ise-extern.fraunhofer.de (S. Kiefer).

<https://doi.org/10.1016/j.jpowsour.2025.238815>

Received 11 August 2025; Received in revised form 24 October 2025; Accepted 8 November 2025

0378-7753/© 2025 The Authors. Published by Elsevier B.V. This is an open access article under the CC BY license (<http://creativecommons.org/licenses/by/4.0/>).

interpretable and transferable model parameters, directly linking operating conditions to aging factors and corresponding aging parameters. These insights not only enhance predictive capability but also support the design of optimized battery management strategies aimed at mitigating dominant aging conditions.

1. Introduction

Batteries are central to modern technology, enabling applications from electric vehicles and renewable energy storage to consumer electronics. Demand for high-performance batteries is expected to continue growing [1]; therefore, understanding the complexities of their aging behavior, which directly impacts their performance and lifespan, is crucial.

Battery aging is characterized by two primary conditions: calendar aging, which occurs over time regardless of usage, and cycle aging, which results from the repeated charging and discharging of the battery [2]. Understanding and predicting these aging processes is vital for optimizing battery applications, as they influence key performance metrics such as capacity, resistance, and overall longevity [3]. Comprehensive insights into battery aging are essential for industries relying on batteries, enabling better management strategies and ultimately enhancing user satisfaction.

Battery aging is shaped by many factors such as mechanical stress, chemical reactions, temperature, and cycling conditions [3,4]. Because these factors interact in complex ways, it is difficult to predict battery behavior across different conditions [2]. Robust models are therefore needed to reliably forecast battery life and performance and support better management decisions.

Battery aging models serve as critical tools in understanding and predicting the degradation mechanisms of batteries. These models can significantly enhance battery health management by allowing operators to adjust operational windows based on the predicted impacts of aging factors [5]. Current approaches often rely on semi-empirical, empirical, physical, and data-driven machine learning techniques, each with its strengths and limitations [6,7]. However, many existing models excel in performance predictions yet fall short in providing interpretable insights into the contributions of specific aging factors.

The primary objective of this paper is to introduce an intuitive and generic battery aging model that not only simulates aging behavior but also quantifies the impact of various stress factors, including temperature (T), state of charge (SOC), depth of discharge (DOD), and current rate (C-rate). By validating this approach with experimental data, this research aims to fill a critical gap in the existing literature, where many models lack interpretability regarding aging contributions. The significance of this study lies in its potential to advance battery technology and management practices, providing a clearer understanding of the quantitative contribution of certain stress factors to battery aging.

2. Battery aging

2.1. Calendar aging

Calendar aging refers to the degradation of battery performance over time, even when the battery is not in use or under load. This phenomenon is primarily influenced by factors such as temperature, SOC, and the chemical composition of the battery materials [8]. During calendar aging, various electrochemical processes, including electrolyte decomposition and solid electrolyte interphase (SEI) growth, contribute to capacity loss and increased internal resistance [4]. Research has shown that elevated temperatures accelerate these aging processes, leading to a significant reduction in the battery's lifespan [9,10]. Capacity fade over time t is often modeled using a power law, resulting in functions for the capacity fade of the form:

$$C(t) = C_0 - \alpha t^\beta \quad (1)$$

where C_0 is the initial capacity and $C(t)$ represents the capacity at time t . α describes the rate of capacity decrease in terms of the storage conditions temperature and state of charge [11,12]. The exponent β is usually used to capture the cell's behavior regarding the growth of the SEI at the graphite anode [11] and is primarily defined by the SOC. The values assigned to β are usually between $\beta = 0.5$ and $\beta = 1$ for diffusion-limited reactions, like SEI growth and accelerated degradation by self-passivation, respectively [13].

One fundamental model to describe the battery's temperature dependence is the Arrhenius equation, which relates the rate of chemical reactions to temperature:

$$k = A \cdot e^{-\frac{E_a}{RT}} \quad (2)$$

where k is the reaction rate constant, A is the pre-exponential factor, E_a is the activation energy, R is the universal gas constant, and T is the absolute temperature in Kelvin.

2.2. Cycle aging

While calendar aging occurs when the battery is not under load, cycle aging refers to the degradation in battery performance caused by repeated cycling.

This phenomenon is primarily influenced by factors such as DOD, C-rate, T, and SOC. During cycling, capacity loss and increased internal resistance result from a combination of mechanical stress reactions, such as particle cracking, and electrochemical processes, including lithium plating, electrolyte decomposition, and the growth of the SEI [4]. Research has shown that deeper discharges and higher current rates can accelerate these aging processes, leading to a significant reduction in the battery's lifespan [14]. Several mathematical models are commonly used to describe the degradation processes associated with cycle aging. One fundamental model is the empirical capacity fade model, which can be expressed as:

$$C(n) = C_0 - r \cdot n \quad (3)$$

where $C(n)$ is the capacity after n cycles (or equivalent full cycles (EFCs) or Ah-throughput), C_0 is the initial capacity, and r is the capacity fade rate per cycle. The capacity fade rate takes into account the investigated stress factors T , SOC , DOD , and $C-rate$.

Recent studies have focused on quantifying the effects of different environmental and charging conditions on calendar and cyclic aging in order to develop battery models. This can provide valuable insights for the optimization of battery design and usage in various applications.

2.3. Aging models

The existing literature presents a range of modeling approaches with different levels of complexity, each addressing specific aspects of battery aging. The predominant aging models can be classified into three categories: empirical, semi-empirical, and physical-based models [6].

Empirical models are based exclusively on experimental data, focusing on fitting predictive outcomes to observed measurements without elucidating the underlying mechanisms [2]. In comparison, semi-empirical models integrate theoretical and physical mechanisms with empirical data to validate or estimate the model parameters [6]. Physical models, on the other hand, are grounded in the fundamental physical laws and principles that govern system behavior, aiming to elucidate the dynamics of physical and chemical reactions occurring within the battery. Complementary to these lifetime models, deep-learning-based approaches for predicting remaining useful life (RUL) have recently gained attention due to their ability to exploit heterogeneous operational features for accurate prognostics [7,15].

These modeling approaches are represented in varying degrees within the literature, each utilizing distinct parameters and equations tailored to different battery chemistries.

Vermeer et al. [2] conducted a comprehensive review of empirical and semi-empirical methodologies for lithium-ion batteries (LIBs). They identified over 40 models, spanning various chemistries including lithium iron phosphate (LFP), lithium nickel manganese cobalt oxide (NMC), lithium nickel cobalt aluminum oxide (NCA), lithium manganese oxide (LMO), and lithium cobalt oxide (LCO), with approximately one-fourth focused on NMC batteries.

Most studies concur that the identified stress factors are prevalent. However, the majority focus on the combined effects of cycle and calendar aging rather than isolating individual contributions. This collective approach obscures the individual contributions of specific stress factors to battery aging. Only a limited number of studies have attempted to quantify and elucidate the effects of individual stress factor ranges on NMC battery aging.

Wang et al. [16] constructed a semi-empirical model for NMC-LMO cells using a test matrix for accelerated cycle life studies covering temperature, C-rate, and DOD. They investigated the capacity and power loss with respect to cycle number, charge throughput, and time by decoupling cycle and calendar life loss. The results showed that calendar aging parameters followed a square-root-of-time dependence with Arrhenius temperature scaling, while cycle aging parameters scaled exponentially with C-rate. By mapping how the loss functions' extracted pre-exponential and exponential factors varied with temperature conditions, they were able to directly relate model coefficients to specific stress factor levels. They showed that the pre-exponential factor scales in a U-shaped manner with a minimum around room temperature while the exponential factor decreases with increasing temperature. Although this work revealed parameter sensitivities with respect to temperature, the study did not discuss in detail the influence of C-rate and DOD on the model parameters. Additionally, the framework was ultimately oriented toward overall life loss rather than isolating the effects of individual stress factors.

Schmalstieg et al. [17] parameterized an aging model for NMC/graphite cells by systematically varying storage temperature, storage SOC, DOD, and mean SOC. They explicitly fitted degradation functions to each test condition before analyzing how the resulting parameters changed with operating variables. For calendar aging, they found that the rate constants increased linearly with voltage and exponentially with temperature, confirming SOC and temperature dependence. For cycling, they found that capacity fade coefficients increased approximately linearly with DOD, while the parameters scaled with average SOC in a quadratic dependency, showing minimum degradation around mid-SOC. In this way, their study linked stress factors to parameter shifts in the model. However, in order to assess the aging factor's behavior, the remaining factors were maintained at fixed levels. The study's focus remained on integrating these dependencies into an aggregate lifetime prognosis tool, without isolating and discussing the impact of each aging factor in the stress factor range.

Cordoba-Arenas et al. [18] developed semi-empirical models for capacity and power fade in NMC-LMO pouch cells under plug-in hybrid vehicle duty cycles. They quantified stress factor influence by extracting severity factors for each experiment and fitting empirical relationships between these factors and operating conditions. Capacity fade parameters were shown to follow an Arrhenius temperature dependence, with additional functional relationships to minimum SOC and charge-sustaining versus charge-depleting duty cycle ratio. In contrast, resistance growth parameters depended linearly on throughput and varied systematically with temperature and C-rate. Importantly, they mapped parameter changes onto SOC and duty cycle conditions, thereby tailoring the model for control-oriented applications. Yet, the isolated contribution of individual stress factor ranges for NMC systems was not fully resolved.

Baghdadi et al. [19] proposed a combined calendar and cycle aging model for NMC-LMO and NCA cells based on Dakin's degradation approach. The influence of stress factors was quantified through controlled experiments: calendar aging was assessed at varying temperatures and SOCs, while cycle aging was evaluated under different C-rates, DODs, and temperatures. Aging rates were obtained from linear fits of logarithmic capacity fade and resistance growth, and subsequently mapped to temperature and SOC using an Arrhenius-type relation. To isolate cycling-induced degradation, calendar contributions were subtracted, revealing that both higher DOD and larger current magnitude accelerate capacity fade. Although this work provided a first quantitative mappings between stress factors and aging rates, the mapping was completed only for calendar aging, leaving the full model incomplete.

In addition to the aforementioned investigations on NMC cells, Karger et al. [20] developed a mechanistic cycle aging model parameterized using cycling data from 59 commercial NCA cells with silicon-graphite anodes. Their methodology separated degradation modes by applying half-cell fitting to open-circuit potential curves, followed by a stepwise algorithm that linked component-specific degradation rates to cycling stress factors such as DOD, mean SOC, temperature, and C-rate. This approach systematically disentangled the contributions of different stress factors, offering new mechanistic insights into how operating conditions influence distinct degradation pathways. However, their work was restricted to NCA chemistry and focused on component-level cycle aging rather than full-cell degradation behavior.

Overall, these studies demonstrated that model parameters are not static but evolve with operating conditions such as SOC, temperature, C-rate, and DOD. While they provided a first mapping of the fitted parameters varied across stress ranges, none of them explicitly disentangled and quantified comprehensively the isolated contribution of individual aging factors over their stress factor ranges for NMC cells.

The present study seeks to address this gap by isolating and quantifying the parameter variations attributable to individual stress factor ranges in NMC cells. By disentangling these contributions, we provide clearer insight into how specific conditions accelerate degradation, thereby advancing the understanding of battery aging beyond cumulative modeling approaches.

3. Methods

The proposed framework follows a stepwise structure that links experimental time series data to interpretable aging parameters. First, the collection of the experimental dataset is introduced. Subsequently, stress factors such as temperature, SOC, DOD, and C-rate are extracted from the raw data. Next, we describe the mathematical formulation of the calendar and cycle aging contributions, where the cycle aging terms act as amplification factors relative to a defined baseline aging rate. Finally, the global parameters of the model are optimized against measured state-of-health (SOH) trajectories to ensure that the framework reproduces experimental outcomes with high accuracy. This stepwise structure is intended to guide the reader from raw input data to the fully parameterized model. Table 2 summarizes the process flow for every stage of the methodological framework and the elements for the corresponding methods.

3.1. Experimental battery aging tests

For conducting this aging study, a set of 20 commercial NMC523/graphite pouch cells with a nominal capacity of 64 Ah were tested under various calendar and cycling conditions. The data was first published in [21]. The original names, "DDF", were changed to "Cell", while preserving the original numbering. An overview of the different test conditions can be found in Table 1. A time- and EFC-weighted violin plot of the time series can be found in the Supplementary Information (Fig. S1).

Table 1Summary of the test conditions. Cells 18–20 were cycled with constant power during charging (CP_{ch}) and discharging (CP_{dis}).

	Name	Temperature (°C)	Mean SOC (%)	DOD (%)	C-rate
Calendar	Cell 1	10	85	–	–
	Cell 2	20	50	–	–
	Cell 3	40	25	–	–
	Cell 4	40	50	–	–
	Cell 5	40	75	–	–
	Cell 6	40	85	–	–
	Cell 7	40	85	–	–
	Cell 8	40	100	–	–
	Cell 15	20	85	–	–
	Cell 16	20	85	–	–
	Cycling	Cell 9	40	47.5	75
Cell 10		20	47.5–77.5	15 - 75	0.5
Cell 11		10	47.5	75	0.5
Cell 12		20	47.5	75	0.5
Cell 13		20	10–90	20	0.5
Cell 14		20	47.5	75	0.25–0.75
Cell 17		25	Load profile		
Cell 18		30	57.5	55	0.5 (CP_{ch}) 2 (CP_{dis})
Cell 19		25	57.5	55	2 (CP_{ch}) 0.5 (CP_{dis})
Cell 20		10	70	30	2 (CP_{ch}) 0.9 (CP_{dis})

The cells underwent regular check-ups in which a quasi-open-circuit voltage (qOCV) with a low current of $C/20$ and a pulse test with varying C-rates were performed to examine the cell capacity and internal resistance. For the cycling cells, the complete battery cycle life was recorded and provided for the battery model. For calendar-aged cells, only the check-ups were recorded and a constant temperature and SOC during the storage period were assumed.

The relative capacity is calculated using Eq. (4)

$$SOH = \frac{C_n}{C_0} = 1 - \Delta SOH \quad (4)$$

where C_n and C_0 represent the capacities at the n th and the initial check-up test, respectively.

3.2. Data preprocessing

The initial step involves calculating the SOC of the batteries using Coulomb counting based on Eqs. (5) and (6), which is subsequently adjusted by comparing the SOC values derived from the relaxation period of the pulse tests against those obtained from the qOCV curve to account for the error accumulation resulting from Coulomb counting.

$$\Delta SOC = \frac{I \cdot \Delta t}{C_0 \cdot SOH \cdot 3600} \quad (5)$$

with I being the current, Δt the time interval in seconds, and C_0 the initial capacity.

$$SOC = SOC_0 + \sum_{i=1}^N \Delta SOC_i \quad (6)$$

where SOC_0 is the initial state of charge, ΔSOC_i is the change in SOC for each interval, and N is the number of intervals.

While the SOC represents the electrical charge level of a battery relative to its full capacity, the DOD is introduced to account for the influence of mechanical stress arising when the cell undergoes contraction/expansion from its relaxed state due to (de-)lithiation. Both positive and negative displacements are assumed to contribute equally to stress accumulation. The DOD is therefore treated as a positive parameter that increases when the battery is charged or discharged. After each significant change in current direction (charge/discharge), the DOD resets to zero again. In contrast to the SOC, the DOD is not a continuous function.

To capture the battery behavior during non-continuous cycling phases and to distinguish between significant (macro) and minor (micro) cycling events, three approaches are applied. The resulting DOD profiles are schematically illustrated in Fig. 1.

1. Distinction between charging and discharging periods (Range Counting):

- During continuous charging or discharging operations, the DOD increases progressively.
- The DOD is reset when a change in the direction of current flow occurs, specifically during the transition from charging to discharging or vice versa.
- The DOD can be represented in terms of the change in SOC, ΔSOC_i , over each of the N intervals as

$$DOD := \begin{cases} \sum_{i=1}^N |\Delta SOC_i|, & \text{if } \text{sgn}(\Delta SOC_i) = \text{sgn}(\Delta SOC_{i-1}), \\ 0, & \text{if } \text{sgn}(\Delta SOC_i) \neq \text{sgn}(\Delta SOC_{i-1}). \end{cases} \quad (7)$$

2. Distinction between macro and micro cycles:

- Macro cycles refer to substantial charging or discharging events that extend across multiple consecutive time intervals, resulting in an SOC difference $> 2\%$.
- Micro cycles are characterized by short-term fluctuations in charging or discharging, typically occurring during breaks or between two macro cycles. The SOC difference within a micro cycle is $\leq 2\%$.

The delimitation and termination of a micro cycle are based on the following criteria:

(a) Macro cycle threshold (Rainflow method):

- A micro cycle concludes when the last SOC value of the preceding macro cycle is exceeded (for a charge macro cycle) or undercut (for a discharge macro cycle).
- Within a macro cycle, the DOD exhibits a monotonically increasing trend.
- The DOD is reset at the start of micro cycles and when transitioning between charging and discharging macro cycles.
- The DOD is not reset after a long cycling break.

(b) Return of previous current direction:

- A micro cycle terminates when the direction of current flow from the last macro cycle is restored.

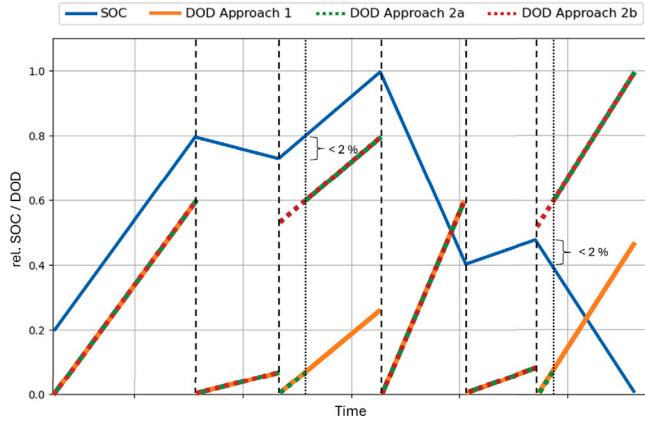


Fig. 1. Schematic representation of the approaches used to derive the depth of discharge from the state of charge. Black dashed lines indicate the change in current direction, black dotted lines indicate the end of micro cycles.

- Similar to the previous method, the DOD is reset at the start of micro cycles and when transitioning between charging and discharging macro cycles.
- While the DOD is calculated successively, it does not necessarily follow a monotonous increase within a cycle, as the DOD value after a micro cycle is determined based on the recent SOC — regardless of the SOC of the previous macro cycle.
- The DOD is not reset after a long cycling break.

The C-rate, which describes the current rate at which the battery is cycled, is calculated as the applied current I divided by the battery's nominal capacity C_0 :

$$C_{rate} = \frac{I}{C_0} \quad (8)$$

Subsequently, data reduction is performed by retaining only significant changes, specifically those meeting the following criteria: $\Delta T \geq 1^\circ\text{C}$, $\Delta U \geq 0.05\text{ V}$, $\Delta I \geq 1\text{ A}$, or $\Delta t \geq 30\text{ s}$.

3.3. Model specification

The capacity loss of batteries over time is modeled as the cumulative effect of calendar aging and cycle aging, expressed in terms of equivalent full cycles:

$$\Delta SOH = f_{cyc} \cdot \Delta EFC + f_{cal} \cdot \Delta t \quad (9)$$

The calendar aging factor, f_{cal} , is defined as:

$$f_{cal} = -\frac{\alpha\beta}{t_{ref}^\beta} \cdot t^{(\beta-1)} \quad (10)$$

This expression is based on established assumptions in the literature as described in Section 2.1, and represents the derivative of Eq. (1) with respect to time t . The term $t_{ref} = 5 \cdot 365.25 \cdot 24 \cdot 3600\text{ [s]}$ is introduced to accurately represent the term $\alpha(SOC, T)$, which denotes the capacity loss after the reference time, t_{ref} (here defined as 5 years). The parameter β characterizes the shape of the aging curve, restricted within the range $0.5 \leq \beta \leq 1$. The combined aging effect of SOC and T is represented in α as:

$$\alpha(SOC, T) = f_\alpha(SOC) \cdot f_\alpha(T) \quad (11)$$

with lookup table (LUT) and linear interpolation for the SOC dependence

$$f_\alpha(SOC) = a_{\alpha, SOC_i} + \frac{(a_{\alpha, SOC_{i+1}} - a_{\alpha, SOC_i})}{(SOC_{i+1} - SOC_i)} \cdot (SOC - SOC_i),$$

$$\text{with } 10^{-9} \leq a_{\alpha, SOC_x} \leq 100 \quad (12)$$

and an exponential equation for the influence of temperature

$$f_\alpha(T) = a_{T_\alpha} \cdot e^{\left(\frac{T}{b_{T_\alpha}}\right)}, \quad \text{with } 0 < a_{T_\alpha} \leq 5 \text{ and } 10^{-9} \leq b_{T_\alpha} \leq 10^9 \quad (13)$$

The parameter β depends only on the SOC and is defined by a LUT similar to $f_\alpha(SOC)$.

$$\beta(SOC) = b_{\beta, SOC_i} + \frac{(b_{\beta, SOC_{i+1}} - b_{\beta, SOC_i})}{(SOC_{i+1} - SOC_i)} \cdot (SOC - SOC_i),$$

with $0.5 \leq b_{\beta, SOC_x} \leq 1$ (14)

For the cycle aging factor, f_{cyc} , multiplicative aging factors are applied to account for interdependencies:

$$f_{cyc} = a_{base} \cdot f(T) \cdot f(SOC) \cdot f(C_{rate}) \cdot f(DOD), \quad \text{with } a_{base} = -\frac{0.2}{7000} \quad (15)$$

This equation provides a framework for understanding the various stress factors, namely T , SOC , DOD , C -rate, that contribute to battery aging as amplification factors, i.e., aging factors ($f(x)$). In this context, a_{base} represents a baseline aging rate, which quantifies the minimal degradation of the battery when it operates under optimal conditions. An initial value of 20% capacity loss over 7000 EFCs is selected. This baseline serves as a reference point, allowing normalization of the cycling factors.

By incorporating these factors into the equation, it becomes possible to assess how deviations from optimal conditions amplify or mitigate the aging process. The use of a_{base} not only facilitates the comparison of aging rates across different operational scenarios, but also helps to identify whether the initial approximation of aging was conservative or overestimated. This approach improves the understanding of the interplay between various operational parameters and their combined effects.

The cycle equations are based on established assumptions from physical chemistry (Arrhenius-like) [11,13], and fracture mechanics (cyclic stress and failure (S-N) curves introduced by Wöhler) [22,23]. For parameters that cannot be derived through physical or chemical knowledge, linear or quadratic LUTs and interpolation are employed to maintain their flexibility.

It is possible to exclude some cycling parameters from the optimization process, in case they have not been varied in the test conditions and they cannot be inferred. In that case, the respective factor will be set to 1, i.e., not being able to affect the value of f_{cyc} .

The aging factors contributing to cycle aging based on the corresponding stress factors are represented in the Eqs. (16)–(19).

For the temperature dependency a LUT with quadratic interpolation is used, rather than directly applying the Arrhenius equation. While the quadratic interpolation is still based on Arrhenius principles, it allows for more effective and direct incorporation and interpretation of empirical data, capturing the complex and nonlinear relationship of temperature effects. This approach facilitates the modeling of variations in temperature conditions, including negative degrees Celsius, while still reflecting the underlying Arrhenius behavior.

$$f(T) = a_{T_i} \cdot \frac{(T - T_{i+1})(T - T_{i+2})}{(T_i - T_{i+1})(T_i - T_{i+2})} + a_{T_{i+1}} \cdot \frac{(T - T_i)(T - T_{i+2})}{(T_{i+1} - T_i)(T_{i+1} - T_{i+2})} + a_{T_{i+2}} \cdot \frac{(T - T_i)(T - T_{i+1})}{(T_{i+2} - T_i)(T_{i+2} - T_{i+1})},$$

with $1 \leq a_{T_x} \leq 100$ (16)

The influence of the SOC is modeled using a LUT with linear interpolation:

$$f(SOC) = a_{SOC_i} + \frac{(a_{SOC_{i+1}} - a_{SOC_i})}{(SOC_{i+1} - SOC_i)} \cdot (SOC - SOC_i),$$

with $1 \leq a_{SOC_x} \leq 100$ (17)

The effects of the DOD and C-rate are expressed through power law functions to represent the characteristics of fracture mechanics:

$$f(DOD) = a_{DOD} \cdot DOD^{b_{DOD}} + 1, \quad (18)$$

with $0 \leq a_{DOD} \leq 5$ and $0 \leq b_{DOD} \leq 100$

$$f(C_{rate}) = a_{C_{rate}} \cdot C_{rate}^{b_{C_{rate}}} + 1, \quad (19)$$

with $0 \leq a_{C_{rate}} \leq 5$ and $0 \leq b_{C_{rate}} \leq 100$

3.4. Optimization and parameter estimation

The optimization is carried out using the least-squares algorithm included in the SciPy optimize module. The calendar-aged cells are weighted by a factor of 2.5 to account for the lower number of data points compared to the cycled cells. The cost function, which is minimized using the local optimizer, is as follows:

$$f_{cost}(\theta) = \sum_{k=1}^K \sum_{n=1}^{N(k)} w_k (q_n - f_n(k, \theta))^2 \quad (20)$$

where q_n represents the measured capacity check-up points with the total number N per cell. K is the total number of cells tested and w_k is the weighting factor. The expression $f_n(k, \theta)$ is the prediction of the model based on the input of aging factors for the specific cell and the model parameters θ .

Model parameterization typically involves keeping all but one stress factor constant [17,20], thereby isolating that condition. This method facilitates a controlled examination of the effects of individual variables on battery aging. In contrast, our approach considers all conditions simultaneously, offering a more holistic approach for defining the interactions among various factors.

The optimized aging parameters are considered global for the whole dataset, as they are constant for the model. However, aging factors can change with varying cycling and storage conditions at every point in the time series and are therefore called local.

3.5. Evaluation strategy

For validation, Cell17 was cycled using a realistic load profile and is not included in the dataset used to find the optimized model parameters. In a second approach, only the first two-thirds of the data points in the datasets are used to fit the model to the existing data, so the last third can be used for validation. The time series show differences in the time intervals of the tests and in the breaks between the tests. Some cells were even exposed to varied stress factor ranges during their cycle life (see Table 1). Therefore, it is valid to assume that it is sufficient to split the data of the individual cells into training and validation sections.

To ensure the robustness of the results, three complementary strategies are employed and are schematically illustrated in Fig. 2. In the first approach, the initial parameter values are optimized simultaneously, guided by trends reported in literature. Specifically, parameters are initialized such that the contribution increases with higher values of SOC, DOD, C-rate, and temperature. This approach tests whether the optimization converges reliably when the starting point is aligned with prior experimental and modeling evidence. In the second strategy, all initial parameters are kept constant without embedding any assumed trend. The optimization is then carried out simultaneously across all parameters. This method serves as a contrast to the first, as it removes any directional bias from the initialization and therefore demonstrates whether the optimization process itself can uncover systematic patterns. The third strategy follows the stepwise procedure proposed by Karger et al. [20]. Here, only a subset of parameters is optimized in each iteration. The parameters for the factors with the lowest mean absolute error (MAE, Eq. (21)) of a subset are fixed as new initial

values, and the process is repeated for the remaining subsets. This is carried out for both constant initials and initials including an assumed trend. The sequential approach reduces the complexity of the optimization at each step and makes it possible to investigate how parameter interdependencies evolve throughout the procedure. In all three strategies, the initial values are deliberately chosen close to the lower boundary of the permissible optimization range. This design ensures comparability across the approaches and prevents convergence from being artificially biased by excessively high starting points.

To formalize the error metric, the mean absolute error is defined as:

$$MAE = \frac{1}{\sum_{k=1}^K N(k)} \sum_{k=1}^K \sum_{n=1}^{N(k)} |y_n - f_n(k, \theta)| \quad (21)$$

where N is the number of capacity check-up points for a number of K tested cells. y_n represents the measured capacity and $f_n(k, \theta)$ the simulated capacity at a certain point. A table with the employed initials can be found in the [Supplementary Information](#).

4. Results and discussion

This section first presents the parameterization results and compares the simulated outcomes with experimental data. We then validate the model using independent datasets and partitioned training data, before analyzing its sensitivity to the definition of DOD, initial parameters, and input conditions. Finally, we discuss the limitations of the framework. This structure moves from overall accuracy to factor-specific insights, ensuring a balanced evaluation of model performance and innovation.

4.1. Model parameterization

The identified model parameters, interpolation points, and investigated ranges are listed in the [Supplementary Information](#).

The simulated aging over time based on the optimized parameters is shown in Fig. 3. The simulation reaches an accuracy of 1.10% MAE and a maximum absolute error of 5.29%. The MAE is lower for the calendar cells (0.40%), meaning that those cells are better represented by the model, while the cycled cells show an MAE of 1.36%. This difference is most likely due to the emphasis of calendar cells during the optimization process. However, it can also be seen that the model better represents a more linear aging behavior, resulting in lower absolute errors. The curves showing a negative square-root decay have higher absolute errors.

Fig. 4 represents the outcome for the aging parameters over the tested stress factor ranges. The results indicate that, for calendar aging, the SOC plays a crucial role in influencing the aging process of battery cells. Specifically, the impact on aging during storage increases with rising SOC levels and temperature. It is noteworthy that the effect of SOC reaches a peak at 85%, after which its influence decreases again as it approaches 100%. This behavior suggests that while intermediate SOC levels can contribute moderately to battery health, higher SOC levels may lead to detrimental effects. A similar pattern is observed during cycle aging, where the SOC initially appears to have little to no effect until it reaches a peak value of 4.04 at 85% SOC, indicating a threshold beyond which the aging process is significantly affected. Previous studies typically report that higher SOC accelerates battery aging, as elevated voltage promotes side reactions and degradation processes. These include SEI growth, electrolyte oxidation, and dissolution of transition metals from the cathode, resulting in loss of active material (LAM) [24–27]. All of which contribute to capacity fade.

However, the test results do not entirely align with this trend reported in literature. Beyond a certain SOC, the aging factor does not consistently increase further. The decay after 85% SOC can either be caused by too little data, as most cells reached an SOC above 85% only during the check-ups. Only one cell was stored at an SOC of 100% and only one cell was partially cycled above 85% in specific sections. However, Krupp et al. [24] observed that, in the context of calendar

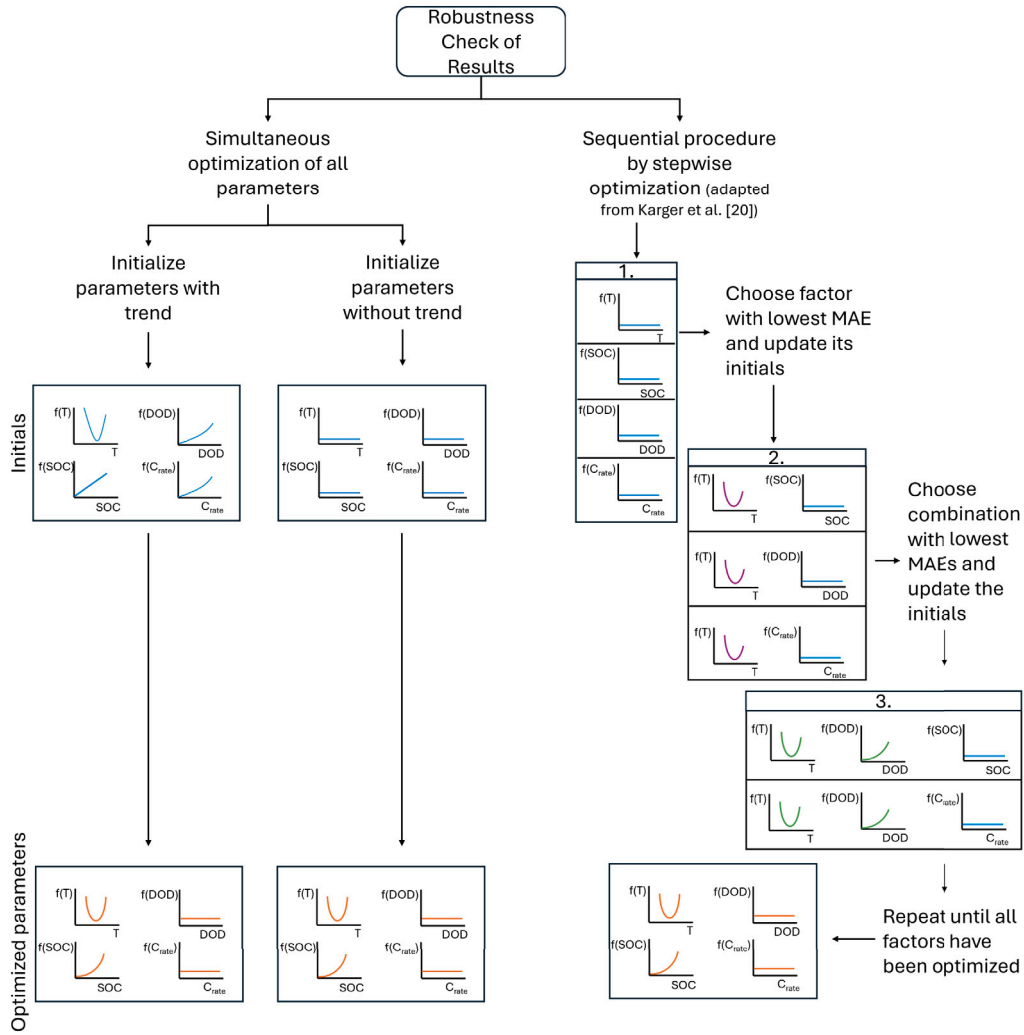


Fig. 2. Schematic representation of the three paths for the robustness check via simultaneous optimization and stepwise approach. The color coding is as follows: blue - pristine initials (i.e., chosen by authors), orange - final optimized parameters, other - interim optimized parameters used as new initials. The sequential optimization method was introduced by Karger et al. [20]. For this approach, only the path with constant initials is represented. However, the same method was also applied for initials with assumed trend. (For interpretation of the references to color in this figure legend, the reader is referred to the web version of this article.)

Table 2
Overview of the computational flow and expressions.

Stage	Elements	Description	Reference
Input	Measurement	time series: temperature $T(t)$, current $I(t)$, voltage $U(t)$, time t , cycles EFC	Experimental [21]
	Data preprocessing	Stress factors SOC(t) from Coulomb counting DOD(t) by three candidate methods C-rate(t) from applied current Data reduction	Eq. (5) Section 3.2 Eq. (8)
Model	Local aging factors	Calendar aging factor $f_{cal}(t)$ with $\alpha(SOC, T)$, $\beta(SOC)$ Cycle aging factor f_{cyc} with a_{base} , $f(T)$, $f(SOC)$, $f(DOD)$, $f(C_{rate})$	Eqs. (10)–(14) Eq. (15) Eqs. (16)–(19)
	SOH determination	$SOH_{k+1} = SOH_k + f_{cyc}(EFC_{k+1}) \Delta EFC + f_{cal}(t_{k+1}) \Delta t$	Eqs. (4), (9)
Optimization	Cost function	Parameter fitting via optimizer loop using least-squares algorithm in SciPy optimize	Eq. (20) Section 3.4
Output	Global aging parameters	Optimized model parameters for aging factors	Table S2
Verification		Out-of-sample testing, Robustness check	Section 3.5 Fig. 2

aging, a cell stored at 90% SOC exhibited similar or even lower aging than one stored at 70% SOC. This suggests that higher SOC levels do not necessarily result in increased capacity loss. A comparable pattern was reported by Di Prima et al. [28], who found that aging peaked at 95% SOC and then decreased for cells at full charge. They attributed this behavior to the shuttle effect between the electrodes, as proposed by Zülke et al. [29] for LIBs with NCA cathode. In this mechanism, ions that would typically contribute to SEI formation are instead redirected toward the cathode, thus mitigating degradation at the anode [28,29].

Furthermore, the analysis reveals that calendar aging decreases with reduced storage temperatures, while a temperature of 20 °C proves to be the most favorable condition during cycling, confirming literature findings [9,13,25,27,30]. At this temperature, an optimal balance between reaction kinetics and thermal stability is achieved, minimizing the adverse effects of elevated temperatures that can accelerate degradation processes [31].

By employing a multiplicative approach to assess aging factors as amplification factors, we move beyond a linear summation approach. This enables normalization of the parameters in the cycle aging term $f_{cyc} = a_{base} \cdot f(T) \cdot f(SOC) \cdot f(Crate) \cdot f(DOD)$ (Eq. (15)) after optimization by adjusting the baseline aging rate, a_{base} , with respect to the minimum values of the individual aging factor functions. The minimum values for the aging factors were analytically derived from the respective functions (Eq. (16)–(19)) as $f_{min}(SOC) = f_{min}(Crate) = f_{min}(DOD) = 1$, indicating that under optimal conditions these parameters neither decrease nor increase the aging rate relative to the baseline. Only $f_{min}(T)$, the minimum of the temperature factor, was identified to be $f_{min}(T) = 0.99$. This deviation from unity reflects the observation that under the most favorable thermal conditions, the aging contribution is marginally lower than the assumed baseline of $a_{base} = -\frac{0.2}{7000}$, leading to $f_{cyc,min} = a_{base} \cdot f_{min}(T) \cdot f_{min}(SOC) \cdot f_{min}(Crate) \cdot f_{min}(DOD) = -\frac{0.2}{7000} \cdot 0.99 \cdot 1 \cdot 1 \cdot 1$. Consequently, to ensure consistency and comparability across all aging factors, the baseline aging rate a_{base} is therefore rescaled to account for this value. The resulting correction $a_{base} = -\frac{0.2}{7000} \cdot 0.99$ indicates that the initially suggested aging rate of 20% capacity loss over 7000 EFCs was only slightly overestimated and can be adjusted to 19.8% for normalization. This normalization allows to directly quantify the contributions of individual stress factors to the overall cycle aging in a consistent framework, which has so far only been addressed in a fragmented or limited manner in literature [16–20].

Among the various stress factors examined, the DOD factor emerges as the most impactful, increasing with higher DOD levels and exhibiting a maximal influence of $f_{max}(DOD) = 6$. This finding aligns with previous studies conducted by Soto et al. [32] and Thien et al. [33], which reported an increase in lifespan for micro-cycled batteries, suggesting that careful management of the DOD can enhance battery longevity. The literature further supports the observation that an increased DOD accelerates aging due to larger fluctuations in electrode volume [34]. Mechanistically, high DOD cycles induce substantial volumetric changes in electrode materials, particularly in the graphite anode and NMC cathode, due to deep lithiation and delithiation [35, 36]. These repeated expansions and contractions generate mechanical stress, leading to the propagation and enlargement of microcracks within the electrode structure [34]. These cracks diminish electronic and ionic conductivity by disrupting the structural integrity and reducing the effective contact area between active materials. Furthermore, the newly exposed surfaces from cracking accelerate the formation of additional SEI, consuming cyclable lithium and contributing to the loss of lithium inventory (LLI) [4,37,38]. These degradation pathways, i.e., mechanical fracturing, SEI growth, and LLI, are central to reductions in capacity over the battery's cycle life [4,34].

Interestingly, the analysis also reveals that the C-rate, defined as the current rate at which the battery is charged or discharged, does not exhibit any significant impact on aging within the tested range. This

holds true even when considering the C-rate parameters for charging and discharging individually (Fig. S2).

The proposed stressor-resolved time series framework was compared to widely used empirical and semi-empirical Refs. [16–19]. Prior works establish Arrhenius-type calendar dependencies and monotonic SOC/DOD effects under controlled matrices, typically varying one factor at a time and aggregating results into lifetime tools. In contrast, our formulation quantifies time-resolved contributions $f(T)$, $f(SOC)$, $f(DOD)$, and $f(Crate)$ directly along the entire time series dataset. The multiplicative structure with normalization facilitates clear isolation of individual factors and ensures consistent scaling across operating ranges. In contrast to mechanistic separation of modes or components [11,20], the present framework addresses full-cell behavior in NMC chemistry and extends naturally to realistic, dynamic load profiles. This enables time-resolved attribution of stressor contributions, a capability not typically achievable with matrix-based fitting approaches [16–20].

The time-resolved contributions of the different factors are depicted for Cell 10 in Fig. 5. The figure illustrates the voltage profile and SOH evolution of the cell under varying DOD conditions, together with the time-resolved progression of different aging factors. In the uppermost panel, the voltage profile reveals the applied DOD regimes, with the lowest DOD of 15% occurring in the blue-shaded region, followed by progressively higher DOD windows of 30%, 45%, 60%, and 75%, indicated by green, gray, yellow, and red backgrounds, respectively. The contributions of calendar aging (f_{cal} , dark purple) and cycle aging (f_{cyc} , green) are shown in the subsequent panel. The calendar aging factor is characterized by a stronger negative contribution at early times that becomes less pronounced as time progresses, leading to a larger ΔSOH initially and a smaller ΔSOH at later stages. In contrast, the cycle aging factor does not evolve monotonically with time but instead responds primarily to changes in cycling conditions, most notably the imposed DOD.

The lower panels depict the multiplicative modifiers of the cycle aging factor, namely the contributions associated with temperature ($f(T)$, red), state of charge ($f(SOC)$, cyan), depth of discharge ($f(DOD)$, pink), and current rate ($f(Crate)$, brown). The weighted cumulative contribution, displayed on the secondary y-axis, evolves over time, with each contribution scaled by the respective ΔEFC . Values equal to unity indicate a neutral effect (i.e., no deviation from baseline aging), while deviations from unity accumulate over time and EFC. Since all modifiers act as multiplicative scaling terms relative to the baseline cycle-aging rate, a_{base} , the cumulative contribution is dimensionless and provides a normalized representation of the aggregated stress impact throughout the aging process.

The temperature factor $f(T)$ does not exhibit a distinct temporal trend but increases with elevated temperature. The factor $f(SOC)$ remains consistently high under all conditions. This behavior arises from the way the DOD was varied: the upper voltage limit was kept constant, while only the lower limit was adjusted. As a result, the SOC regularly reached the critical threshold of 85% in every cycle, yielding the largest cumulative impact on cycle aging (588 over the testing period). The DOD factor $f(DOD)$ shows pronounced peaks during check-up phases and contributes notably during high-DOD operation (yellow and red zones). In contrast, $f(Crate)$ remains constant at unity, indicating no measurable effect under the applied cycling conditions.

A key advantage of this method compared to conventional approaches is its ability to resolve the shown time-dependent contribution of individual stress factors. Whereas many aging models provide only averaged or lumped effects over extended periods, this approach enables a direct visualization of how each factor evolves under dynamic operating conditions. This not only improves interpretability but also allows for a more accurate attribution of degradation mechanisms to specific usage patterns, thereby offering a more detailed and mechanistically grounded perspective on cell aging.

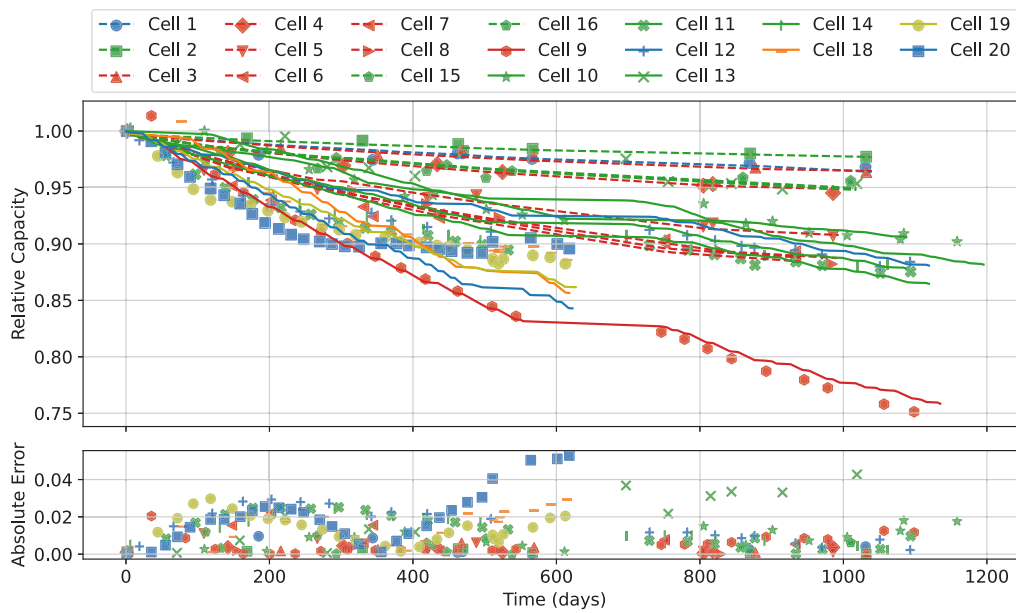


Fig. 3. Simulated SOH (line) and measured SOH retrieved from check-up tests (scatter) over time. The lower scatter plot indicates the absolute error for each capacity point. Calendar cells are depicted by dashed lines, cycle-aged cells by solid lines. The color indicates the temperature, where blue, green, and red correspond to 10 °C, 20 °C, and 40 °C, respectively. (For interpretation of the references to color in this figure legend, the reader is referred to the web version of this article.)

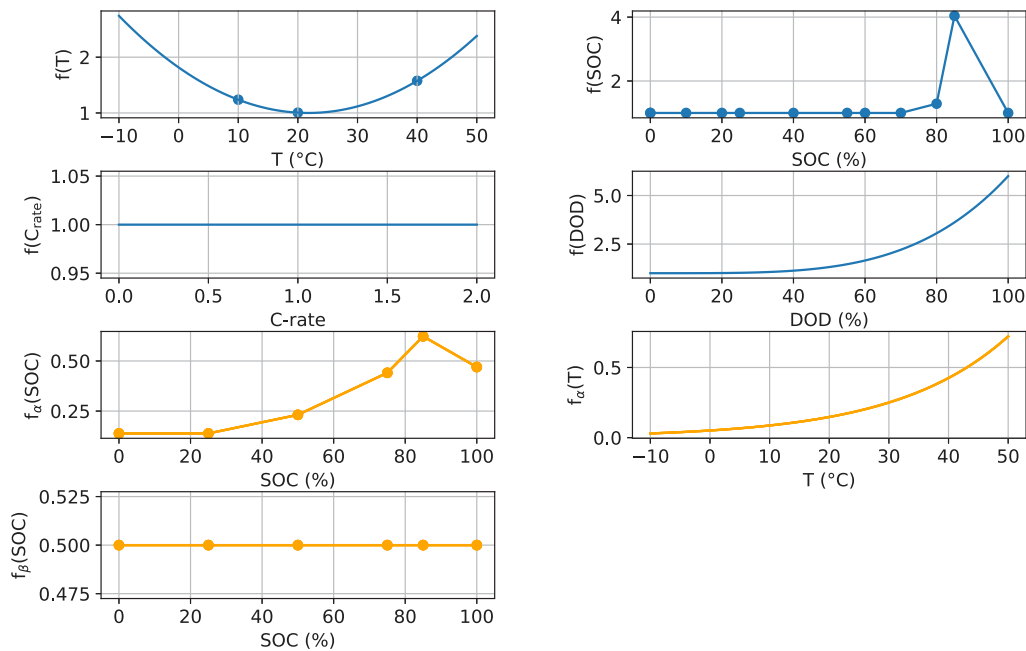


Fig. 4. Relationships between aging factors and their associated stress factors within the tested ranges. Calendar aging factors are depicted in orange, while cycle aging factors are represented in blue. (For interpretation of the references to color in this figure legend, the reader is referred to the web version of this article.)

Overall, the figure highlights the quantitative and cumulative effects of distinct stress factors, namely SOC, temperature, DOD, and C-rate, on the long-term degradation of cell performance over the tested operation period. These results provide valuable insights into the complex interactions among aging mechanisms and their implications for developing battery management strategies aimed at extending both the lifetime and performance of battery systems.

In the existing literature, it has been demonstrated that the aging of calendar-aged batteries undergoing periodic capacity checks is inherently related to cycle aging [39,40]. Tests performed on cells subjected to infrequent assessments, in contrast to calendar-aged cells receiving

regular evaluations, revealed significant differences in capacity decline and resistance increase. These findings indicate that calendar and cycle aging cannot simply be summed. To investigate to which extent this affects the proposed model, we compare the outcomes of the pure calendar model based solely on calendar cells with the calendar parameters from the entire dataset. A comparison of Figs. 4 and 6 shows that the derived calendar parameters exhibit only minor differences in the SOC dependence. This means that while we acknowledge the findings in the literature regarding the distinct effects of calendar and cycle aging, our model, which operates on a summation basis, can be considered sufficiently accurate for practical purposes.

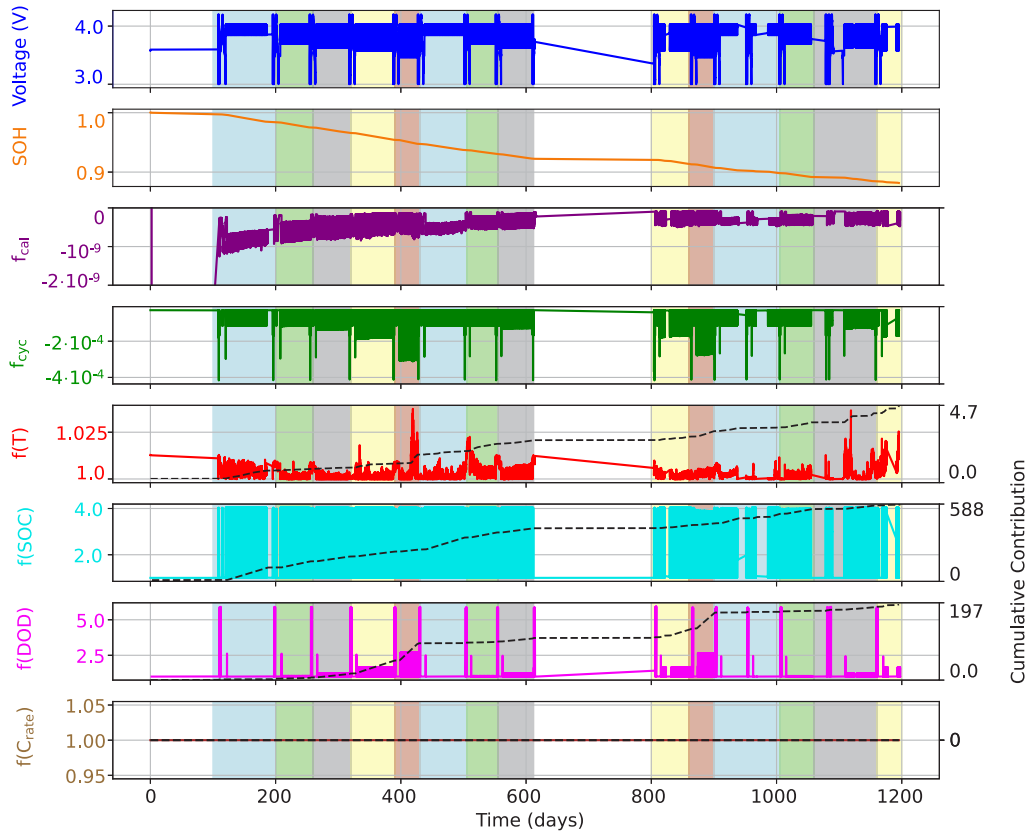


Fig. 5. Contribution of the aging factors over time for Cell 10 (DOD varied cell). The upper panels show the voltage profile across the different applied DOD conditions and the corresponding SOH, which exhibits a gradual decline. Subsequent plots illustrate various aging factors (solid lines) for the investigated stress factors, namely temperature, SOC, DOD, and C-rate. The dashed line depicts the weighted cumulative contribution of the factors when differing from unity. Background shading highlights the applied DOD levels: 15% (blue), 30% (green), 45% (gray), 60% (yellow), and 75% (red). (For interpretation of the references to color in this figure legend, the reader is referred to the web version of this article.)

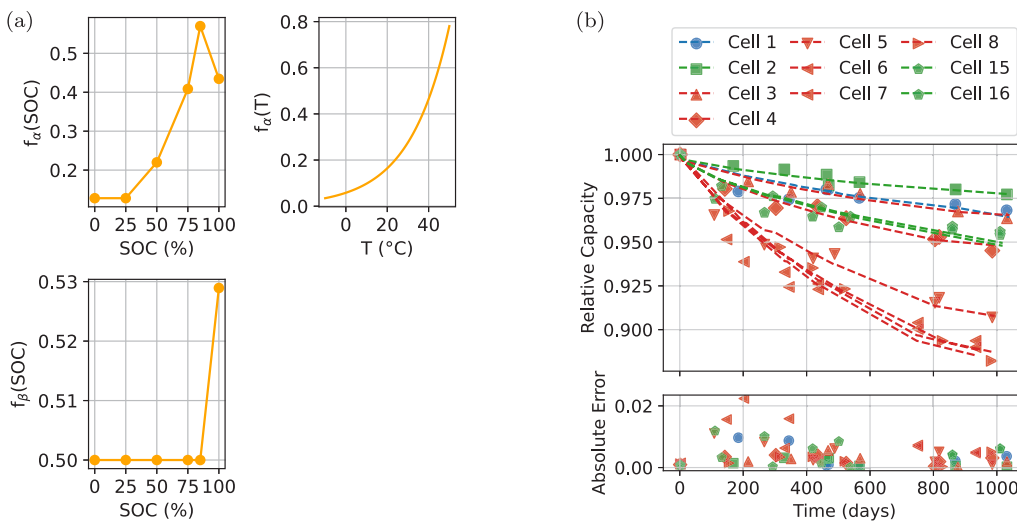


Fig. 6. (a) Relationships between the calendar aging factors and their corresponding stress factor for the calendar cells in the tested ranges. Each subplot presents the impact of the respective stress factor on the aging characteristics of the system, highlighting the dependencies observed in the data. (b) Simulated SOH (line) and measured SOH retrieved from check-up tests (scatter) over time for the calendar cells. The lower scatter plot indicates the absolute error for each capacity point.

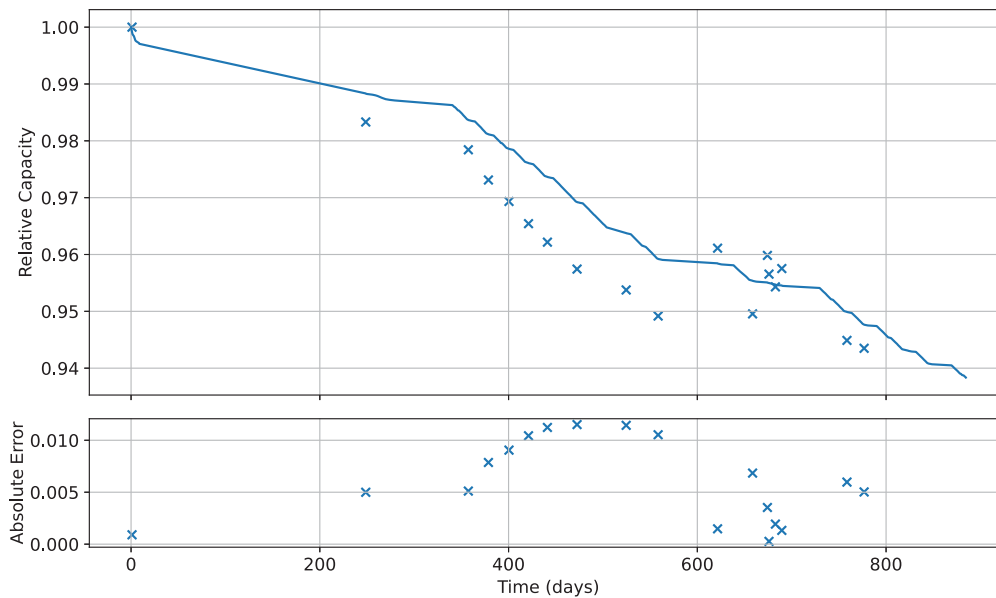


Fig. 7. Simulated SOH (line) and measured SOH retrieved from check-up tests (scatter) over time for Cell 17, which was cycled under load profile. The lower scatter plot indicates the absolute error for each capacity point.

4.2. Model validation

To validate the findings for the aging parameters, we used two different approaches. First, the cell cycled under load profile was excluded from the input data used for optimization. This method allows to assess the model's predictive capabilities independently, ensuring that the optimized parameters are robust and not overfitted to the training data.

The results of this validation process are illustrated in Fig. 7, which presents the simulation outcomes for the cell cycled with the load profile based on the optimized parameters.

The simulation results align closely with the measured SOH values, indicating that the model captures the battery's aging behavior based on the cycle life time series data. The lower plot provides further insight into the accuracy of the simulations by displaying the absolute error across the testing period. The validation revealed a maximum absolute error of less than 1.2% and a mean absolute error (MAE) of 0.61% compared to the original measured capacities. These results suggest a high level of accuracy, indicating that the model can reliably predict capacity fading of the tested cells under the specified load profile and generalize well to conditions not included in the training dataset.

In the second approach, we partitioned the data, using two-thirds for training and one-third as a validation set. As detailed in Section 3.5, this method is applicable since a battery's treatment can vary throughout its life due to handling differences. Fig. 8 represents the shortened dataset (solid line) alongside the corresponding validation subset (dashed line). The lower scatter plot indicates the absolute errors. Even though the maximum error is larger in this approach, the results show only a slightly higher MAE of 1.34%, which is 0.24% higher than the MAE obtained using the entire dataset. Cell 17, which was subjected to a load profile during cycling and was not part of the training data, exhibits an MAE of 0.54%. This indicates a performance comparable to the previous method (Fig. 7).

The low mean absolute error values reinforce the credibility of the optimized aging parameters and the overall modeling approach. They also highlight the model's potential for practical applications, such as in battery management systems, where accurate predictions of battery performance are essential to optimize usage and extend lifespan [41].

In conclusion, the validation process demonstrates that the model, based on the optimized aging parameters, can simulate the performance

of lithium-ion cells under realistic cycling conditions with an accuracy in the range of measurement errors. The low mean absolute error values further support the robustness of the findings, providing a solid foundation for future research. However, the cells cycled with constant energy profile (Cells 18–20) showed exceptionally high errors when the split approach was used for validation. This indicated that the model shows sensitivity to some cycling procedures.

Further validation against diverse datasets and operating conditions will be essential to enhance the model's applicability and reliability in real-world scenarios.

4.3. Sensitivity on depth of discharge definition

Existing literature lacks a definitive method for determining the DOD in dynamically cycled systems. Established approaches are derived from fatigue mechanics, such as the Rainflow method and Range Counting [33,42]. Reports of extended lifespans for micro-cycled batteries underscore the significance of this stress factor in the context of battery cycle aging. Thien et al. [33] emphasized the DOD as critical variable in their proposed model.

For the continuously cycled cells, the DOD is identical across all three approaches introduced in Section 3.2 and therefore has no effect on the optimization of aging parameters. For cells subjected to load profiles, however, the calculated DOD can differ depending on the counting method and thus affect the SOH estimation. Nevertheless, the model exhibited only minimal variation among the three approaches. For the dynamically cycled battery (Cell 17), the deviation in SOH between the simplest approach (Range Counting) and the two more detailed methods remained below 0.11%, independent of whether a 2% or 10% SOC threshold was used to define micro cycles.

The deviation of this observation from literature may be attributed to the relatively low DOD (approx. 50%), which falls within a range where the model does not assign a significant impact to the DOD (<1.4). A more pronounced effect of the DOD definition on SOH estimation becomes apparent when the DOD of a micro cycle is maintained at the same value as the terminal DOD of the preceding macro cycle. This indicates that the definition of DOD can have an impact on the SOH estimation. In the case of the tested cycling profile, however, the changes were insignificant.

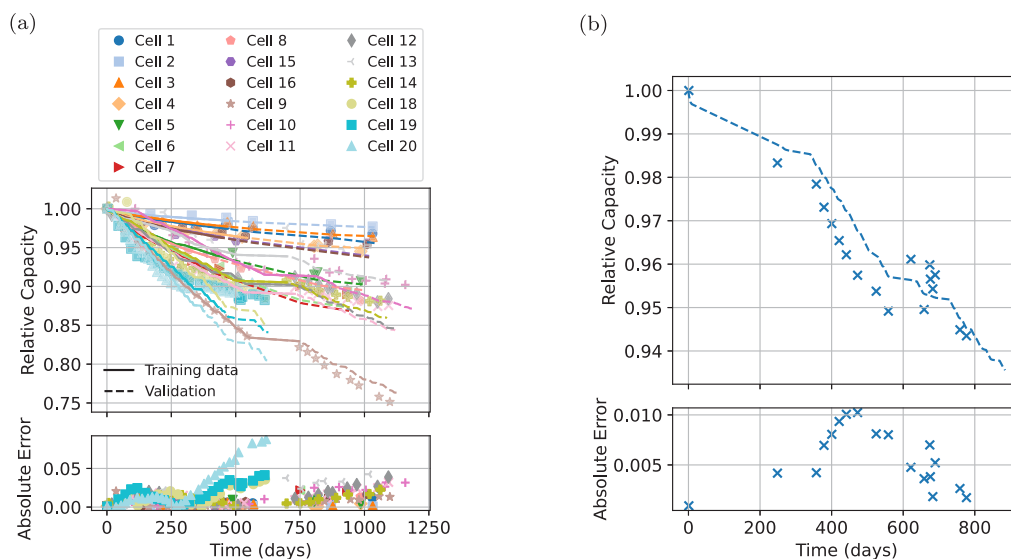


Fig. 8. Simulated SOH (line) and measured SOH retrieved from check-up tests (scatter) over time for the dataset (a) and Cell 17 (b). The solid line indicates the training data, while the dashed line represents the validation data. The lower scatter plot indicates the absolute error for each capacity point.

4.4. Sensitivity on initials and base

The model demonstrates minimal dependence on the selected initial values for optimization. As described in Section 3.5, three approaches were employed to assess their influence. In the selection process, values close to the lower boundary of the permissible optimization range were chosen to avoid distorting the nature of the amplification factors. The optimization results remained qualitatively consistent across all three scenarios, yielding the same MAE, despite showing slight quantitative differences (Fig. S3).

When the constant initial values deviate significantly from moderate levels, the outcomes diverge, resulting in increased MAE (Table S2 in the Supplementary Information). We attribute this deviation to a stronger interaction between the initial values and the trajectory of the optimization process toward a different local minimum, leading to variations in convergence speed or direction. This effect is less pronounced when a trend is employed or the optimization is done stepwise (Table S3, Table S4 in the Supplementary Information). For the stepwise approach, the qualitative results are comparable no matter the employed trends or level of moderation (Figs. S6–S7).

However, a significant deviation from the moderate values contradicts the intended purpose of the factors, which are introduced to enhance effects within a controlled and specific framework. Extreme initial values can distort the intended impact of the optimization and steer the results in undesirable directions.

When the base value, a_{base} , is decreased by a certain factor, the weighted cumulative contribution of the product of cycle aging factors, represented by Eq. (22), tends to increase within the same order of magnitude. This indicates that the base value is a useful reference for normalizing the aging factors.

$$C_{total} = C(EFC_N) = \sum_{i=1}^N \left(\frac{f_{cyc}(EFC_i)}{a_{base}} \cdot \Delta EFC(EFC_i) \right) \quad (22)$$

where $f_{cyc}(EFC_i)$ denotes the cycle-aging parameter at step i , and $\Delta EFC(EFC_i)$ represents the incremental change in equivalent full cycles. The summation is performed over all N steps to obtain the total weighted contribution C_{total} .

However, it is important to highlight that the contribution of the individual stress factors can change. For a reduction of a_{base} with a factor of 10, $f(SOC)$ increases with a factor of 5 and additionally becomes more significant around 20% SOC, while the DOD curve shows

a steeper slope (Fig. S4 in Supplementary Information) and the MAE is reduced to 0.95%. The rise observed at 20% SOC could be attributed to phase transitions in the anode. Differential voltage analysis (DVA) reveals a peak at this SOC level (Fig. S5), indicating the occurrence of a graphite phase transition from stage I to stage II [2].

This means that selecting the appropriate base value is crucial, as it can affect the parameter interpretation.

4.5. Sensitivity on input data

The selection of measurement data for optimization significantly impacts the model. To develop a robust model, it is essential to test and include as many conditions as possible in the optimization process. Data profiles outside the tested range may not be accurately represented, and extrapolating such data can lead to considerable discrepancies and incorrect assumptions.

The issue is most evident when all cells cycled with a constant energy profile (Cells 18–20) are simultaneously excluded from the optimization. In this scenario, the main influence of SOC shifts toward lower charging states, while the impact of the C-rate becomes considerably more pronounced. Due to its power-law dependence, the C-rate factor can reach values as high as 340 at 2 C. Consequently, Cells 18–20, cycled with currents ≥ 1.5 C, experience unrealistic aging rapidly in the validation scenario (Fig. S11).

When only one cell cycled with a constant energy profile is excluded at a time (Cells 18–20), the results indicate variations in the optimization outcomes for the parameters (Supplementary Information, Figs. S8–S10). However, the overall trend remains consistent, allowing qualitative conclusions regarding the primary contributing conditions. Notably, the MAE of the cell cycled under the load profile (Cell 17) changes only slightly — 0.65% as maximal MAE compared to 0.61% when all other cells are included in the optimization. A comprehensive list of all MAEs can be found in Supplementary Information, Table S5.

In conclusion, our model's results are reliable only for conditions within the tested ranges, where interpolation is applicable. For conditions beyond these limits, it is necessary to individually assess whether the influence can be extrapolated. It is crucial to ensure that the extremes of the subsequent application scenarios are adequately covered.

4.6. Limitations

A primary limitation of the presented approach is the missing amplification of severely damaging conditions, particularly in scenarios

involving lithium plating. While we attempted to address this issue through a multiplicative approach, we assume that these methods do not provide adequate amplification when the combination of stress factors is particularly severe, such as in high current, elevated SOC, and low temperature conditions. Under these circumstances, the electrochemical behavior of lithium-ion batteries can deviate significantly from expected performance metrics, leading to potential safety hazards and reduced lifespan [38]. The inability to accurately model these extreme conditions limits the predictive benefit of the simulations and may result in an oversimplification of the complex interactions occurring within the battery system. On the other hand, the Battery Management System (BMS) must prevent such extreme conditions for the aforementioned safety reasons. Therefore, if extreme aging is effectively mitigated, the necessity for modeling it becomes limited.

Additionally, the model does not allow for the representation of potential path dependencies occurring in LIBs [43]. Since it only considers the conditions at a specific point in the time series, it does not allow inferences about current or future predictions based on the history of the cell.

As discussed in Section 4.1, the model utilizes a summation approach to account for both cycle and calendar effects. Existing research suggests that this methodology does not accurately represent the calendar cell aging due to the frequent capacity check-ups [39,40]. However, we believe that incorporating the complete dataset, which includes check-up data for the calendar cells, contributes to a model, which attempts to capture the cycle-aged characteristics of calendar-aged cells.

Another significant limitation is the challenge of representing the knee-point in the capacity versus cycle life curve under constant cycling and calendar conditions. The knee-point, which indicates a transition in the degradation behavior of the battery, is crucial for understanding the long-term performance and reliability of lithium-ion batteries [44–46]. However, the introduced model does not allow for the accurate depiction of this critical behavior. We hypothesize that incorporating resistance as a variable could enhance the model's ability to capture this phenomenon. Nevertheless, the lack of empirical data to validate this approach remains a barrier.

The calculation of the DOD has some disadvantages, particularly with regard to use during operation. Currently, the determination of DOD is based solely on historical data, which means that real-time monitoring of DOD values is not possible and an integration into an Energy Management System (EMS) is difficult.

This study also faced limitations in modeling the possible increase in capacity as the presented model assumes a constant capacity fade throughout the battery's life. This assumption may not reflect the reality of battery behavior, where certain conditions can lead to temporary increases in capacity due to factors such as structural adaptations within the electrode materials [14,47]. The inability to account for these variations restricts the model's accuracy and may lead to misleading conclusions regarding longevity of the battery systems under investigation.

5. Conclusion

This study successfully established a model for predicting the aging behavior of lithium-ion cells, demonstrating robust results with a mean absolute error of 1.10% and maximum absolute errors of 5.29%. Beyond its predictive performance, the key advancement lies in establishing an interpretable, stressor-resolved framework that isolates and quantifies the effects of individual stress factors, namely temperature, SOC, DOD, and C-rate, across the tested operating ranges for the NMC cells.

The findings reveal that the SOC significantly influences aging, particularly when stored at elevated levels, with diminishing adverse effects beyond 85% SOC. Additionally, the DOD emerged as a crucial factor, with higher DOD levels correlating with accelerated aging due

to mechanical stresses impacting electrode integrity. The analysis of aging factors over time revealed that, despite the high absolute impact of DOD, the cumulative sum for SOC is for most cells greater, indicating its consistently high influence throughout the observation period. The C-rate, however, showed negligible influence within the tested parameters.

Validation against a cell cycled under load profile with a mean absolute error of 0.61% further confirmed the reliability of the model, indicating its potential for practical applications in real-world battery management systems.

This study shows how specific operating conditions drive degradation, providing a basis for better battery management strategies. However, challenges remain in modeling suboptimal conditions, knee-points, and non-linear capacity fade. Addressing these aspects will be critical for further enhancing the reliability and applicability of the proposed framework in practical battery technology. These findings demonstrate that the proposed framework can improve both lifetime prediction and the design of management strategies for lithium-ion batteries.

CRedit authorship contribution statement

Samira Kiefer: Writing – original draft, Visualization, Validation, Software, Methodology, Investigation, Formal analysis, Data curation, Conceptualization. **Maximilian Bruch-Rosar:** Writing – review & editing, Supervision, Methodology, Investigation, Data curation, Conceptualization. **Hans-Martin Henning:** Writing – review & editing, Supervision. **Magdalena Graczyk-Zajac:** Writing – review & editing, Supervision, Project administration, Funding acquisition.

Declaration of Generative AI and AI-assisted technologies in the writing process

During the preparation of this work the authors used AI-supported language models in order to enhance language and readability. After using this tool, the authors reviewed and edited the content as needed and take full responsibility for the content of the published article.

Declaration of competing interest

The authors declare that they have no known competing financial interests or personal relationships that could have appeared to influence the work reported in this paper.

Acknowledgments

The data was collected as part of the project DDD-BATMAN funded by MarTERA, Research Council of Norway (RCN, Contract No. 311445), and German Federal Ministry of Economic Affairs and Energy (Grant No. 03SX525B). The work on the aging model was carried out as part of the project ResHy funded by German Federal Ministry for Economic Affairs and Energy (Grant No. 03EI4058).

Appendix A. Supplementary data

Supplementary data to this article can be found online at <https://doi.org/10.1016/j.jpowsour.2025.238815>.

Data availability

Data will be made available on request.

References

- [1] T. Hettesheimer, C. Neef, I.R. Inclán, S. Link, T. Schmaltz, F. Schuckert, A. Stephan, M. Stephan, A. Thielmann, L. Weymann, T. Wicke, Lithium-Ion Battery Roadmap – Industrialization Perspectives Toward 2030, Tech. rep., 2023, <http://dx.doi.org/10.24406/publica-2153>.
- [2] W. Vermeer, G.R.C. Mouli, P. Bauer, A comprehensive review on the characteristics and modeling of lithium-ion battery aging, *IEEE Trans. Transp. Electrification* 8 (2022) 2205–2232, <http://dx.doi.org/10.1109/TTE.2021.3138357>.
- [3] S. Ding, Y. Li, H. Dai, L. Wang, X. He, Accurate model parameter identification to boost precise aging prediction of lithium-ion batteries: A review, *Adv. Energy Mater.* 13 (2023) <http://dx.doi.org/10.1002/aenm.202301452>.
- [4] C.R. Birkl, M.R. Roberts, E. McTurk, P.G. Bruce, D.A. Howey, Degradation diagnostics for lithium ion cells, *J. Power Sources* 341 (2017) 373–386, <http://dx.doi.org/10.1016/j.jpowsour.2016.12.011>.
- [5] Y. Wang, H. Xiang, Y.Y. Soo, X. Fan, Aging mechanisms, prognostics and management for lithium-ion batteries: Recent advances, *Renew. Sustain. Energy Rev.* 207 (2025) <http://dx.doi.org/10.1016/j.rser.2024.114915>.
- [6] C. Miller, M. Goutham, X. Chen, P.D. Hanumalagutti, R. Blaser, S. Stockar, A semi-empirical approach to a physically based aging model for home energy management systems, in: 2022 IEEE Conference on Control Technology and Applications, CCTA 2022, Institute of Electrical and Electronics Engineers Inc., 2022, pp. 165–170, <http://dx.doi.org/10.1109/CCTA49430.2022.9966091>.
- [7] S. Wang, S. Jin, D. Bai, Y. Fan, H. Shi, C. Fernandez, A critical review of improved deep learning methods for the remaining useful life prediction of lithium-ion batteries, *Energy Rep.* 7 (2021) 5562–5574, <http://dx.doi.org/10.1016/j.egypr.2021.08.182>.
- [8] J. Vetter, P. Novák, M.R. Wagner, C. Veit, K.C. Möller, J.O. Besenhard, M. Winter, M. Wohlfahrt-Mehrens, C. Vogler, A. Hammouche, Ageing mechanisms in lithium-ion batteries, *J. Power Sources* 147 (2005) 269–281, <http://dx.doi.org/10.1016/j.jpowsour.2005.01.006>.
- [9] K. Jalkanen, J. Karppinen, L. Skogström, T. Laurila, M. Nisula, K. Vuoriolehto, Cycle aging of commercial NMC/graphite pouch cells at different temperatures, *Appl. Energy* 154 (2015) 160–172, <http://dx.doi.org/10.1016/j.apenergy.2015.04.110>.
- [10] M. Broussely, S. Herreyre, P. Biensan, P. Kasztejna, K. Nechev, R.J. Staniewicz, Aging mechanism in Li ion cells and calendar life predictions, *J. Power Sources* 97–98 (2001) 13–21, [http://dx.doi.org/10.1016/S0378-7753\(01\)00722-4](http://dx.doi.org/10.1016/S0378-7753(01)00722-4).
- [11] A. Karger, J. Schmitt, C. Kirst, J.P. Singer, L. Wildfeuer, A. Jossen, Mechanistic calendar aging model for lithium-ion batteries, *J. Power Sources* 578 (2023) <http://dx.doi.org/10.1016/j.jpowsour.2023.233208>.
- [12] P. Gasper, K. Gering, E. Dufek, K. Smith, Challenging practices of algebraic battery life models through statistical validation and model identification via machine-learning, *J. Electrochem. Soc.* 168 (2021) 020502, <http://dx.doi.org/10.1149/1945-7111/abddel>.
- [13] V.N. Lam, X. Cui, F. Stroebel, M. Uppaluri, S. Onori, W.C. Chueh, A decade of insights: Delving into calendar aging trends and implications, *Joule* 9 (2025) <http://dx.doi.org/10.1016/j.joule.2024.11.013>.
- [14] J. Guo, Y. Li, J. Meng, K. Pedersen, L. Gurevich, D.I. Stroe, Understanding the mechanism of capacity increase during early cycling of commercial NMC/graphite lithium-ion batteries, *J. Energy Chem.* 74 (2022) 34–44, <http://dx.doi.org/10.1016/j.jechem.2022.07.005>.
- [15] S. Wang, Y. Fan, S. Jin, P. Takyi-Aninakwa, C. Fernandez, Improved anti-noise adaptive long short-term memory neural network modeling for the robust remaining useful life prediction of lithium-ion batteries, *Reliab. Eng. Syst. Saf.* 230 (2023) <http://dx.doi.org/10.1016/j.res.2022.108920>.
- [16] J. Wang, J. Purewal, P. Liu, J. Hicks-Garner, S. Soukiazian, E. Sherman, A. Sorenson, L. Vu, H. Tataria, M.W. Verbrugge, Degradation of lithium ion batteries employing graphite negatives and nickel-cobalt-manganese oxide + spinel manganese oxide positives: Part 1, aging mechanisms and life estimation, *J. Power Sources* 269 (2014) 937–948, <http://dx.doi.org/10.1016/j.jpowsour.2014.07.030>.
- [17] J. Schmalstieg, S. Käbitz, M. Ecker, D.U. Sauer, A holistic aging model for Li(NiMnCo)O₂ based 18650 lithium-ion batteries, *J. Power Sources* 257 (2014) 325–334, <http://dx.doi.org/10.1016/j.jpowsour.2014.02.012>.
- [18] A. Cordoba-Arenas, S. Onori, Y. Guezennec, G. Rizzoni, Capacity and power fade cycle-life model for plug-in hybrid electric vehicle lithium-ion battery cells containing blended spinel and layered-oxide positive electrodes, *J. Power Sources* 278 (2015) 473–483, <http://dx.doi.org/10.1016/j.jpowsour.2014.12.047>.
- [19] I. Baghdadi, O. Briat, J.Y. Delétage, P. Gyan, J.M. Vinassa, Lithium battery aging model based on dakin's degradation approach, *J. Power Sources* 325 (2016) 273–285, <http://dx.doi.org/10.1016/j.jpowsour.2016.06.036>.
- [20] A. Karger, J. Schmitt, C. Kirst, J.P. Singer, L. Wildfeuer, A. Jossen, Mechanistic cycle aging model for the open-circuit voltage curve of lithium-ion batteries, *J. Power Sources* 593 (2024) 233947, <http://dx.doi.org/10.1016/j.jpowsour.2023.233947>.
- [21] E. Vanem, Q. Liang, M. Bruch, A. Bakdi, Ø.Å. Alnes, Data-informed state of health estimation for maritime lithium-ion battery systems using an ensemble of simple linear models, *J. Mar. Eng. Technol.* (2024) 1–17, <http://dx.doi.org/10.1080/20464177.2024.2440983>.
- [22] J. Fleer, S. Zurmühlen, J. Badedá, P. Stenzel, J.F. Hake, D.U. Sauer, Model-based economic assessment of stationary battery systems providing primary control reserve, in: *Energy Procedia*, vol. 99, Elsevier Ltd, 2016, pp. 11–24, <http://dx.doi.org/10.1016/j.egypro.2016.10.093>.
- [23] S. Qin Hou, J. Quan Xu, Relationship among S-N curves corresponding to different mean stresses or stress ratios, *J. Zhejiang Univ.: Sci. A* 16 (2015) 885–893, <http://dx.doi.org/10.1631/jzus.A1400321>.
- [24] A. Krupp, R. Beckmann, T. Diekmann, E. Ferg, F. Schuldt, C. Agert, Calendar aging model for lithium-ion batteries considering the influence of cell characterization, *J. Energy Storage* 45 (2022) 103506, <http://dx.doi.org/10.1016/j.est.2021.103506>.
- [25] B. Rumberg, B. Epding, I. Stradtmann, M. Schleder, A. Kwade, Holistic calendar aging model parametrization concept for lifetime prediction of graphite/NMC lithium-ion cells, *J. Energy Storage* 30 (2020) 101510, <http://dx.doi.org/10.1016/j.est.2020.101510>.
- [26] E. Wikner, E. Björklund, J. Fridner, D. Brandell, T. Thiringer, How the utilised SOC window in commercial Li-ion pouch cells influence battery ageing, *J. Power Sources Adv.* 8 (2021) 100054, <http://dx.doi.org/10.1016/j.powera.2021.100054>.
- [27] P. Keil, S.F. Schuster, J. Wilhelm, J. Travi, A. Hauser, R.C. Karl, A. Jossen, Calendar aging of lithium-ion batteries, *J. Electrochem. Soc.* 163 (2016) A1872–A1880, <http://dx.doi.org/10.1149/2.0411609jes>.
- [28] P. Di Prima, D. Dessantis, D. Versaci, J. Amici, S. Bodoardo, M. Santarelli, Understanding calendar aging degradation in cylindrical lithium-ion cell: A novel pseudo-4-dimensional electrochemical-thermal model, *Appl. Energy* 377 (2025) 124640, <http://dx.doi.org/10.1016/j.apenergy.2024.124640>.
- [29] A. Zülke, Y. Li, P. Keil, R. Burrell, S. Belaisch, M. Nagarathinam, M.P. Mercer, H.E. Hoster, High-energy nickel-cobalt-aluminium oxide (NCA) cells on idle: Anode- versus cathode-driven side reactions, *Batter. Supercaps* 4 (2021) 934–947, <http://dx.doi.org/10.1002/batt.202100046>.
- [30] L. Wildfeuer, A. Karger, D. Aygül, N. Wassiliadis, A. Jossen, M. Lienkamp, Experimental degradation study of a commercial lithium-ion battery, *J. Power Sources* 560 (2023) 232498, <http://dx.doi.org/10.1016/j.jpowsour.2022.232498>.
- [31] T. Waldmann, M. Wilka, M. Kasper, M. Fleischhammer, M. Wohlfahrt-Mehrens, Temperature dependent ageing mechanisms in lithium-ion batteries - a post-mortem study, *J. Power Sources* 262 (2014) 129–135, <http://dx.doi.org/10.1016/j.jpowsour.2014.03.112>.
- [32] A. Soto, A. Berrueta, M. Mateos, P. Sanchis, A. Ursúa, Impact of micro-cycles on the lifetime of lithium-ion batteries: An experimental study, *J. Energy Storage* 55 (2022) 105343, <http://dx.doi.org/10.1016/j.est.2022.105343>.
- [33] T. Thien, H. Axelsen, M. Merten, D.U. Sauer, Energy management of stationary hybrid battery energy storage systems using the example of a real-world 5 MW hybrid battery storage project in Germany, *J. Energy Storage* 51 (2022) 104257, <http://dx.doi.org/10.1016/j.est.2022.104257>.
- [34] C. Pastor-Fernández, K. Uddin, G.H. Chouchelamane, W.D. Widanage, J. Marco, A comparison between electrochemical impedance spectroscopy and incremental capacity-differential voltage as Li-ion diagnostic techniques to identify and quantify the effects of degradation modes within battery management systems, *J. Power Sources* 360 (2017) 301–318, <http://dx.doi.org/10.1016/j.jpowsour.2017.03.042>.
- [35] W.H. Woodford, W.C. Carter, Y.M. Chiang, Design criteria for electrochemical shock resistant battery electrodes, *Energy Environ. Sci.* 5 (2012) 8014–8024, <http://dx.doi.org/10.1039/c2ee21874g>.
- [36] W.S. Yoon, K.Y. Chung, J. McBreen, X.Q. Yang, A comparative study on structural changes of LiCo_{1/3}Ni_{1/3}Mn_{1/3}O₂ and LiNi_{0.8}Co_{0.15}Al_{0.05}O₂ during first charge using in situ XRD, *Electrochem. Commun.* 8 (2006) 1257–1262, <http://dx.doi.org/10.1016/j.elecom.2006.06.005>.
- [37] A. Maheshwari, M. Heck, M. Santarelli, Cycle aging studies of lithium nickel manganese cobalt oxide-based batteries using electrochemical impedance spectroscopy, *Electrochim. Acta* 273 (2018) 335–348, <http://dx.doi.org/10.1016/j.electacta.2018.04.045>.
- [38] S.F. Schuster, T. Bach, E. Fleder, J. Müller, M. Brand, G. Sextl, A. Jossen, Nonlinear aging characteristics of lithium-ion cells under different operational conditions, *J. Energy Storage* 1 (2015) 44–53, <http://dx.doi.org/10.1016/j.est.2015.05.003>.
- [39] J. Schmitt, A. Maheshwari, M. Heck, S. Lux, M. Vetter, Impedance change and capacity fade of lithium nickel manganese cobalt oxide-based batteries during calendar aging, *J. Power Sources* 353 (2017) 183–194, <http://dx.doi.org/10.1016/j.jpowsour.2017.03.090>.
- [40] A. Karger, S.E.J. O'Kane, M. Rogge, C. Kirst, J.P. Singer, M. Marinescu, G.J. Offer, A. Jossen, Modeling particle versus SEI cracking in lithium-ion battery degradation: Why calendar and cycle aging cannot simply be added, *J. Electrochem. Soc.* 171 (2024) <http://dx.doi.org/10.1149/1945-7111/ad76da>.
- [41] R.R. Kumar, C. Bharatiraja, K. Udhayakumar, S. Devakirubakaran, K.S. Sekar, L. Mihet-Popa, Advances in batteries, battery modeling, battery management system, battery thermal management, SOC, SOH, and charge/discharge characteristics in EV applications, *IEEE Access* 11 (2023) 105761–105809, <http://dx.doi.org/10.1109/ACCESS.2023.3318121>.
- [42] J. Schijve, *Fatigue of Structures and Materials*, Springer Dordrecht, Delft, 2008, <http://dx.doi.org/10.1007/978-1-4020-6808-9>.

- [43] F. Röder, S. Ramasubramanian, A review and perspective on path dependency in batteries, *Energy Technol.* 10 (2022) 2200627, <http://dx.doi.org/10.1002/ente.202200627>.
- [44] T. Wang, Y. Zhu, W. Zhao, Y. Gong, Z. Zhang, W. Gao, Y. Shang, Capacity degradation analysis and knee point prediction for lithium-ion batteries, *Green Energy Intell. Transp.* 3 (2024) 100171, <http://dx.doi.org/10.1016/j.geits.2024.100171>.
- [45] S. Sohn, H.E. Byun, J.H. Lee, CNN-based online diagnosis of knee-point in Li-ion battery capacity fade curve, in: *IFAC-PapersOnLine*, 55, Elsevier B.V., 2022, pp. 181–185, <http://dx.doi.org/10.1016/j.ifacol.2022.07.441>.
- [46] P.M. Attia, A. Bills, F.B. Planella, P. Dechent, G. dos Reis, M. Dubarry, P. Gasper, R. Gilchrist, S. Greenbank, D. Howey, O. Liu, E. Khoo, Y. Preger, A. Soni, S. Sripad, A.G. Stefanopoulou, V. Sulzer, Review—"knees" in lithium-ion battery aging trajectories, *J. Electrochem. Soc.* 169 (2022) 060517, <http://dx.doi.org/10.1149/1945-7111/ac6d13>.
- [47] M. Dubarry, C. Truchot, B.Y. Liaw, Synthesize battery degradation modes via a diagnostic and prognostic model, *J. Power Sources* 219 (2012) 204–216, <http://dx.doi.org/10.1016/j.jpowsour.2012.07.016>.